

Calibration techniques and datatype extraction for time-resolved optical tomography

Elizabeth M. C. Hillman,^{a)} Jeremy C. Hebden, Florian E. W. Schmidt, Simon R. Arridge,^{b)} Martin Schweiger, Hamid Dehghani, and David T. Delpy
Department of Medical Physics, University College London, 11-20 Capper Street, London WC1E 6JA, United Kingdom

(Received 11 January 2000; accepted for publication 6 June 2000)

This article describes the preprocessing and calibration methods currently applied to data acquired with the University College London multichannel time-resolved optical tomography system. We briefly outline the imaging system and describe the features of our experimentally collected data, sources of stochastic noise, and systematic errors. We examine two methods of calibrating data: “difference imaging” using two image data sets with and without the features of interest to produce an image, and “absolute imaging” using an independent calibration measurement. We describe the methods developed to apply each calibration to raw data. Although the difference imaging performed is found to produce images with fewer artifacts, analysis indicates that it will not be directly applicable for clinical applications. Also examined are the effects of using a two dimensional (2D) reconstruction scheme to produce images from measured data. For absolute imaging, artifacts are shown to dominate such images even in the case of a homogeneous third dimension. The feasibility of deriving an *ad-hoc* correction factor to allow the use of a 2D reconstruction for measured data is examined, and is shown to reduce artifact. Difference imaging is demonstrated to be more robust to such effects. © 2000 American Institute of Physics.

[S0034-6748(00)03609-1]

I. INTRODUCTION

As first demonstrated by Jöbsis in 1977,¹ tissue oxygenation can be determined from differences in the characteristic absorptions of oxy- and deoxy-hemoglobin (the oxygenated and deoxygenated forms of hemoglobin, the oxygen carrying component of blood) at optical wavelengths. Biomedical optics research at University College London (UCL) has focused on the potential of optical radiation for monitoring brain function of the human neonate. One avenue of this research has been the development of time-resolved optical tomography as a means of imaging brain function in neonates. As a continuous cotside monitor in an intensive care unit, a functional imaging system could provide early detection of abnormal cerebral oxygenation or perfusion and potentially aid prevention of permanent brain injury.

Optical tomography involves the transillumination of tissue with near infrared (NIR) light (~ 700 – 1000 nm) in order to reconstruct a map of the internal optical properties from measurements made on the tissue surface. Time-resolved optical tomography utilizes the observed dependence on optical properties of the time taken for NIR light to propagate through tissue.² The advantages of time-resolved measurements over simple intensity data include a reduced sensitivity to the effects of light coupling at the tissue surface, and an increased dependence of temporal data on deeper

structures³ together with the ability to separate the effects of absorbers and scatterers.⁴ The UCL prototype 32-channel time-resolved imaging system, the multichannel optoelectronic near-infrared system for time-resolved image reconstruction (MONSTIR) has recently been completed and is described in detail by Schmidt *et al.*⁵ Time-resolved data are acquired by MONSTIR and image reconstructions are performed using an iterative finite element method (FEM) based algorithm, temporal optical absorption and scattering tomography (TOAST) as described by Schweiger and Arridge.⁶

Reliable production of images using the TOAST software requires that the experimental data match the predictions of the forward model as accurately as possible. To achieve this, it has been necessary to devise methods of preprocessing the experimental data to reduce the effects of unavoidable systematic errors. The complexity of the calibration required depends heavily on the type of information being extracted from the measured temporal data. Since many investigators employ only intensity data for image reconstruction, calibration is often performed using a reference object. However for temporal (and frequency domain) data, methods of making calibration measurements and applying them must be carefully considered. This need for detailed calibration in all optical tomography methods is a symptom of the necessity for experimentally collected data to be adequately modeled by either the analytic or numerical methods chosen to produce images. In this article we describe the methods which have been developed to effectively calibrate data from MONSTIR, and substantially reduce the manifestation of image artifacts. Although conventionally “differ-

^{a)}Author to whom correspondence should be addressed; electronic mail: ehillman@medphys.ucl.ac.uk

^{b)}Also with: Department of Computer Science, University College London, Gower Street, London WC1E 6BT, UK.

ence imaging," where a reference data set is used to eliminate features common to the reference and the actual data is often used, we believe that the production of reference phantoms for clinical subjects may prove impractical. Hence the primary objective of this work is to produce images using temporal data without recourse to a reference measurement. This requires calibration methods that can be performed prior to imaging an object of arbitrary shape and optical properties.

A. Imaging principles

When NIR light passes through human tissue, such as the neonatal brain, the overwhelming effects of scatter prohibit the use of the Radon transform and back-projection methods for image reconstruction. The approach adopted at UCL is to measure the temporal distribution of photons transmitted between points on an object's surface in response to illumination by an impulse of light. It is then assumed that a finite set of measurements between pairs of points is sufficient to reconstruct an arbitrary distribution of internal absorbers and scatterers. The TOAST reconstruction package employs a FEM forward model, based on the diffusion approximation to the radiative transfer equation,⁷ which generates simulated measurements for a given distribution of internal scattering and absorbing properties in an object. These values are then compared to measured data and the model is adjusted iteratively until acceptable correspondence between the two is achieved. Thus TOAST is composed of a forward model, an objective function to be minimized, based on the error between model predictions and measured data, and a scheme for adjusting the parameters of the FEM model to achieve minimization.

Other methods developed for tomographic imaging of the internal optical properties of highly scattering objects include the use of frequency domain data. Here, an amplitude modulated source rather than a pulsed source is used.⁸ Each modulation frequency provides the equivalent of one sample of the Fourier transform of a time-resolved data set. Quantitatively accurate images were produced by McBride *et al.*⁹ using frequency domain data and a reference phantom of known composition. Intensity (continuous wave) measurements on phantoms have been used by Jiang *et al.*¹⁰ to produce absorption and scatter maps, although the investigators noted that intensity modulated measurements provided superior images. Again, a homogeneous reference phantom was used to calibrate the data. Meanwhile Ueda *et al.*¹¹ report the reconstruction of images of absorption and scatter in breast phantoms using absolute intensity data without recourse to reference measurements.

B. Data acquisition

The MONSTIR imaging system is illustrated in Fig. 1. Picosecond pulses from a Ti:sapphire laser, operated at a repetition rate of 80 MHz and a wavelength of around 800 nm, are coupled via a fiber switch and one of 32 optical fibers to the surface of the object to be imaged. Light transmitted through the object is collected simultaneously by 32 detector fiber bundles. Each fiber bundle delivers the light to

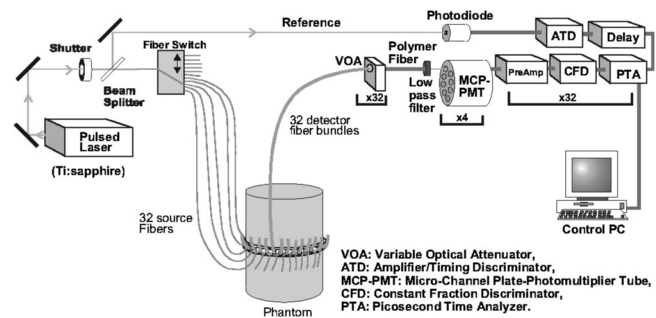


FIG. 1. Schematic diagram of the MONSTIR imaging system.

a variable optical attenuator (VOA) which reduces the risk of damage to the detectors, and decreases the required dynamic range. Light that has passed through the VOA then travels along a short length of wide diameter polymer fiber, and via a visible light blocking long pass filter to the photocathode of one of four eight-anode microchannel-plate (MCP) photomultiplier tubes. A detected photon results in an electronic pulse, which is amplified and converted to a fast nuclear instrument module (NIM) logic pulse by a constant fraction discriminator (CFD). A reference signal derived from pulses split from the main laser beam is also converted into fast NIM logic pulses and delayed by an appropriate amount. The relative delay between the signal from each CFD and the reference signal is then measured by a picosecond time analyzer (PTA) which builds up a histogram of individual photon arrival times. These histograms, or so-called temporal point spread functions (TPSFs), may then be read out from the PTAs by a control PC. A full set of data is collected by sequentially illuminating each of the 32 source fibers and recording the resulting TPSFs for each of the 32 detector bundles for each source. The data set for a single image then comprises up to 1024 TPSFs. The TPSF is the temporal distribution of photons transmitted between points on an object's surface in response to illumination by an impulse of light, as described in Sec. IA.

C. Data extraction

TOAST does not utilize entire TPSFs for reconstruction. Instead, the forward model derives various datatypes, representing characteristics of the TPSF directly, thereby decreasing computational complexity and increasing reconstruction speed. Consequently, preparing data for image reconstructions involves extracting these datatypes from the measured data, and supplying TOAST with the positions of each source and detector. This means that it is essential to extract datatypes from the measured TPSFs that are sufficiently free from systematic sources of noise and uncertainty to provide a good correspondence with those calculated by the forward model. In this article we describe the methods developed for optimizing the extraction of reliable datatypes from experimentally measured TPSFs.

II. EXPERIMENTAL DATA CHARACTERISTICS

The datatypes used in reconstructions must be suitably robust, and the chosen combination must disclose sufficient

information to differentiate between absorption and scatter.⁴ So far, the TPSF datatypes we have most frequently employed for image reconstruction are the mean flight time, variance about the mean (or *central* variance), integrated intensity, and normalized Laplace transform, since they have proven to be effective in reconstruction simulations.^{12,13} In order to extract these datatypes from the experimental data reliably, we must consider the potential sources of error which influence their evaluation.

During the development of MONSTIR substantial improvements in temporal stability were achieved. The width of the system's impulse response has been steadily reduced as a result of careful tuning and electrical interference reduction throughout the instrument. However the system will always have a finite impulse response, certain sources of noise will remain, and some unavoidable temporal drift will occur. The effects of the various sources of stochastic and systematic noise and temporal broadening on a typical TPSF are illustrated in Fig. 2(b). A simulated TPSF from the three-dimensional (3D) forward FEM model for the same geometry, source-detector spacing, and optical properties is shown for comparison [Fig. 2(a)]. Distortions in the measured TPSF shape can be more clearly seen on a logarithmic scale [Fig. 2(c)]. The various sources of distortion and noise are now considered separately below. Each datatype depends to a different degree on each type of noise. It is hence necessary to ensure that the following sources of noise have minimal effect on the calculation of datatypes.

A. Stochastic noise

Temporally uncorrelated noise is evident on all experimentally measured TPSFs [Fig. 2(c1)]. The signal to noise ratio is less for TPSFs collected for larger source-detector separations due to reduction in the intensity of the signal (despite the reduction in dynamic range provided by the VOAs). The background level will also be determined by the individual thresholding properties of each CFD. This background intensity will influence the calculation of experimental datatypes. For example, the existence of apparent photon counts at flight times shorter than that of an unscattered photon will produce an effect on datatypes not accounted for by the forward model.

B. Position and dynamic range dependent features (cross talk)

The fiber switch employed by MONSTIR sequentially couples input from the laser via an optical fiber to one of the 32 source fibers. However leakage of light within the switch into the other 31 nonactivated fibers is around 10^{-8} of the illuminated source intensity. This fraction is comparable to the attenuation across the 7 cm diam tissue-equivalent phantom typically employed for imaging experiments ($\sim 10^{-6}$). Therefore the intensity of light entering a detector bundle from an adjacent nonactivated source fiber can be significant compared to that due to an activated source much further from the detector. Since light from the closer source will have traveled less distance, it will generally arrive before the main TPSF and is evident as a ‘pre’-peak [Fig. 2(c2)]. The occurrence and relative magnitude of prepeaks depend on the

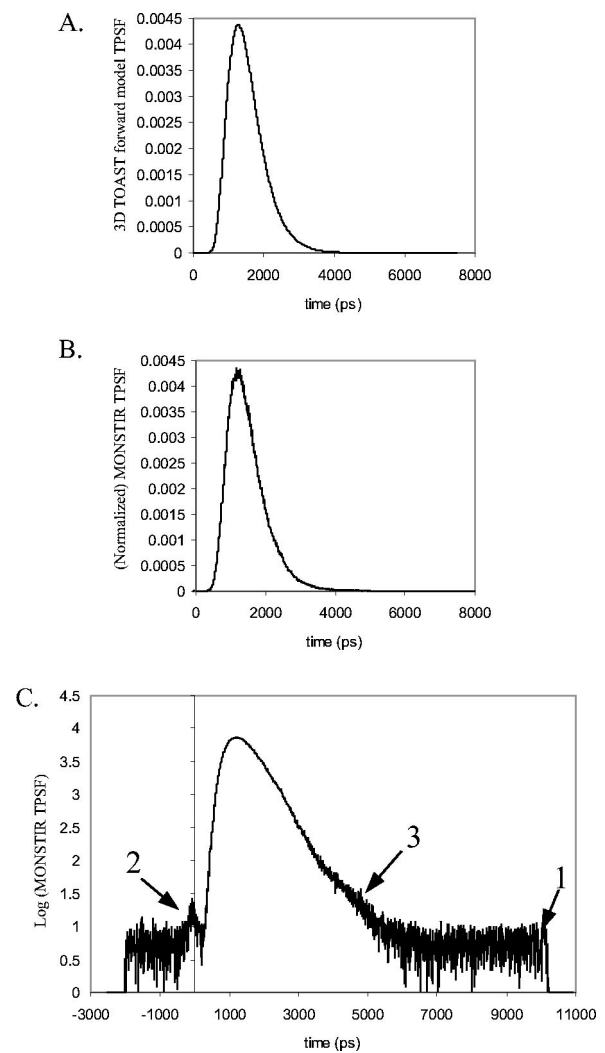


FIG. 2. (a) A TOAST forward model TPSF for the central plane of a homogeneous cylindrical (3D) mesh $\mu'_s = 0.85 \text{ mm}^{-1}$ and $\mu_a = 0.011 \text{ mm}^{-1}$, with 70 mm diam and source-detector separation 47 mm (1.473 rad). (b) A MONSTIR TPSF from the central plane of a solid cylindrical phantom with diameter 70 mm and nominal properties $\mu'_s = 0.85 \pm 0.10 \text{ mm}^{-1}$ and $\mu_a = 0.011 \pm 0.002 \text{ mm}^{-1}$ with a source-detector separation of 47 mm. (c) The TPSF shown in (b), but on a logarithmic scale.

source-detector pair in use, the intensity delivered by the particular source, and the amount of attenuation across the object being imaged. In addition to the prepeak, the use of eight-anode MCPs as described in Sec. IB leads to some ‘cross talk’ between neighboring detector channels ($<0.3\%$). This manifests as a superposition of the TPSFs of the adjacent detector channels. The magnitude of the cross talk is dependent on the relative intensities of the TPSFs for each detector, but since ‘detector 8’ is adjacent to ‘detector 1’, in heavily attenuating media, this cross talk can become significant. Note that through integration of a bank of subsidiary source fiber shutters, the prepeak in the MONSTIR system will soon be significantly reduced. MCP cross talk could also eventually be eliminated via hardware modifications.

C. Source and detector specific features

The variation in lengths and properties of fibers, bundles, and cables, and gradual temporal drifts within the electron-

ics, result in each detector channel having a unique impulse response. In addition, an optical reflection occurs within the MONSTIR system at each end of the short length of polymer fiber between the VOAs and the long pass filters. This is evident as a distortion in the later part of the TPSF [Fig. 2(c3)]. The magnitude of the reflection and its temporal delay relative to the unreflected signal is specific to each detector channel. Also, each source fiber will deliver a pulse with different temporal characteristics due to the fiber switch and the varying lengths and properties of each of the 32 source fibers.

III. USING A REFERENCE PHANTOM MEASUREMENT AS CALIBRATION

A. Difference imaging using temporal datatypes

Measurements made on a reference object are often used to determine absolute optical properties of subsequently measured tissues.¹⁴ Similarly, a well-defined reference object is often employed by researchers in the field of optical tomography to acquire reference data in addition to data collected on the object of interest.¹⁵ The advantage of such a reference measurement is that most systematic errors common to both data sets will be eliminated in the resulting *difference image*. To obtain the reference measurement, a phantom with similar background optical properties and dimensions to the object of interest is used. Alternatively two data sets could be collected at different wavelengths on an object whose structure is known to have different absorptions at each wavelength, or acquired before and after a physiological change. Researchers have also proposed a method of imaging using differential changes in diffuse light transmission following contrast agent administration.¹⁶ Constraints on the properties of such reference measurements are discussed in Sec. IV C.

The ratios of intensity measurements have been shown to produce satisfactory images of phantoms.¹⁵ However, in the clinical environment it may prove difficult to obtain high quality intensity data (or amplitudes for frequency domain), due to the effects of movement, optical coupling to the tissue, and the heightened sensitivity of the datatype to features close to the surface (such as hair).³ Mean flight time and other temporal datatypes are more robust to such effects and are thus potentially more suitable for routine clinical applications. Use of such datatypes also offers the opportunity to unambiguously separate absorption and scatter.⁴ As will be shown in Secs. IV B and IV C, if we create a difference image using mean flight times, we must use the *difference* (not the ratio) of the mean flight times derived from data collected on a reference object and the object of interest.

The reconstructed images shown in Fig. 3 are the eighth iterations of *mean flight time difference images*. MONSTIR was used to acquire TPSFs in the central plane of a cylindrical tissue-equivalent phantom containing a small inhomogeneity with five times the background absorption and scatter. The phantom is 70 mm in diameter and 140 mm in length, and the embedded object is a cylinder 8 mm in diameter, 10 mm tall, and is located 17.5 mm radially from the center, in the plane of the fiber holder ring (as shown in Fig. 1). The

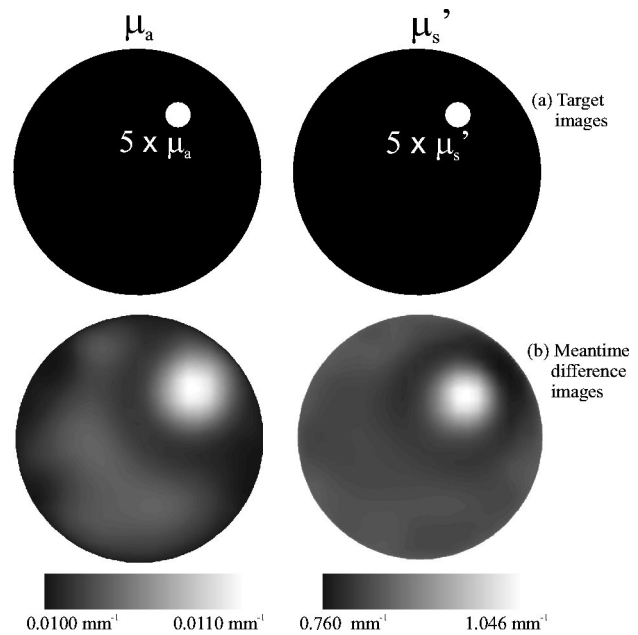


FIG. 3. (a) Target images. (b) Mean time difference reconstructions using a 2D mesh, of experimental data collected on a structured phantom, utilizing a reference measurement on a homogeneous phantom as described in Sec. III A.

estimated average background values for this phantom, found using the method described later in Sec. V B, were $\mu_s' = 0.85 \pm 0.10 \text{ mm}^{-1}$ and $\mu_a = 0.011 \pm 0.002 \text{ mm}^{-1}$ at 800 nm. The reference measurement was collected on a homogeneous cylindrical phantom (diameter 70 mm and height 110 mm) with estimated optical properties of $\mu_s' = 0.9 \pm 0.10 \text{ mm}^{-1}$ and $\mu_a = 0.01 \pm 0.002 \text{ mm}^{-1}$ at 800 nm. The source intensity required to ensure sufficient signal to noise ratio for larger source–detector separations, necessitated the five detectors either side of each source to be blocked by the VOAs. TPSFs were collected for all other source–detector pairs, and hence each data set (image and reference) comprised of 704 mean flight time values. The images were reconstructed using a 2D mesh and utilized no additional calibration information. The mesh contained 3800 nodes, and the starting parameters were $\mu_s' = 0.85 \text{ mm}^{-1}$ and $\mu_a = 0.01 \text{ mm}^{-1}$. The images are scaled linearly from the minimum to the maximum pixel values. The absorbing and scattering inhomogeneity can be clearly seen and there is very little background artifact.

However, although the reference phantom was not exactly matched, as will be shown later in Sec. IV C it is important that the reference object has similar optical properties and dimensions to the object being imaged. A time-resolved system described by Ntziachristos *et al.*¹⁷ requires measurements of a liquid phantom with and without the inhomogeneities to successfully produce difference images. The manufacture of such reference phantoms for use with neonatal subjects is unlikely to prove feasible at the bedside. It is therefore desirable to develop a method of calibrating for the systematic errors described in Sec. II that is effective regardless of the optical properties and geometry of the object being imaged. Attempts to produce images of comparable quality to those achieved using difference imaging have required

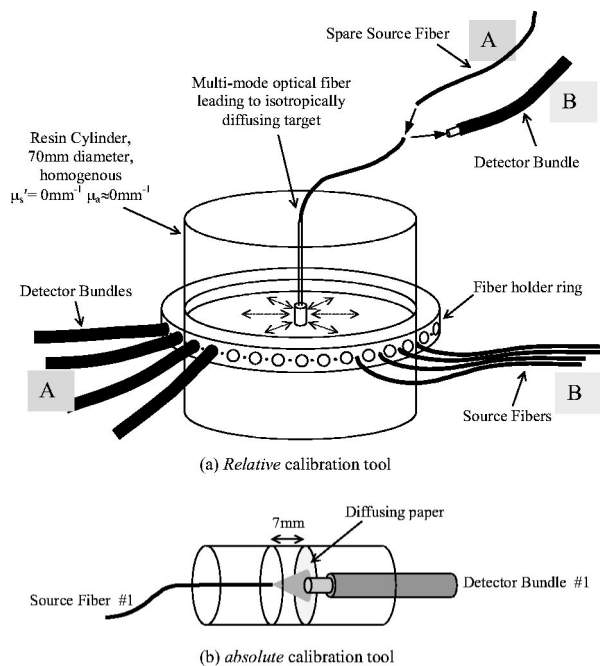


FIG. 4. The *relative* (a) and *absolute* (b) calibration tools used to temporally calibrate variations between different sources and different detector channels, and to evaluate the system's impulse response, as described in Sec. IV A.

development of calibration tools, and methods of applying corrections to measured data.

IV. CALIBRATION AND DATATYPE EXTRACTION WITHOUT A REFERENCE MEASUREMENT

A. Calibration tools and measurements

The greatest potential source of uncertainty in mean flight time is the variation in the lengths of the many optical fibers and electrical cables that make up the system. Reflections and variations in TPSF shape due to the finite instrument response of the system also contribute error, but to a lesser degree. By contrast, central variance is not affected by differences in delay, but is heavily dependent on the TPSF shape.

To facilitate calibration of the system, two calibration tools were constructed as shown in Fig. 4. The source and detector *relative calibration tool* [Fig. 4(a)] is an epoxy resin cylinder of 70 mm diameter. An optical fiber is coupled to a small scattering cylinder embedded in the center. In configuration A, a source fiber from the laser is connected to the central scatterer, providing isotropic illumination of the 32 detector bundles positioned in the central plane. In configuration B, a detector bundle is coupled to the fiber leading to the central scatterer, which then effectively collects any light incident on the central scatterer from each of the 32 source fibers positioned in the central plane. The *absolute calibration tool* [Fig. 4(b)] holds a source fiber and a detector bundle at a known distance apart, shielded from extraneous light and utilizing the beam divergence to illuminate the whole bundle. A small piece of diffusing paper is positioned in front of the bundle to ensure realistic excitation of all the modes in its constituent multimode fibers. Calibration mea-

surements are made each time an image data set is acquired in order to compensate for long-term laser instability and temporal drift in the electronics. We use the tools to perform three separate measurements as follows.

1. Detector calibration

Using configuration (A) as shown in Fig. 4(a), pulsed laser light is delivered to the central diffusing target via a spare source fiber. No light is incident from any of the other source fibers shown around the circumference. The 32 detector bundles are held around the circumference of the tool by a supporting ring (only four are shown for clarity), equidistant from the diffusing target, which provides uniform and roughly equal illumination of all 32 bundles. The MONSTIR system records the TPSFs from all 32 channels when the central target is illuminated. This provides the temporal response of each detector channel to the same incident signal.

2. Source calibration

Using configuration (B) as shown in Fig. 4(a) a detector bundle (No. 1) is coupled to the small diffusing target in the center of the tool. The 32 source fibers are held around the circumference of the tool by the supporting ring (again, only four are shown for clarity), equidistant from the diffusing target. The fiber switch is used to sequentially activate each source fiber, which then illuminates the central target and thus light enters the coupled detector bundle. The MONSTIR system records the TPSF from detector channel No. 1 as each source is activated. This provides the temporal characteristics of each incident source, when collected by the same detector channel.

3. Absolute calibration

Using the tool shown in Fig. 4(b), source fiber No. 1 and detector bundle No. 1 are held at a known separation (7 mm). The system records the TPSF from channel No. 1 when source No. 1 is illuminated. This measures the temporal response of detector No. 1 to source No. 1.

B. Elimination of source and detector specific temporal response variations

The conventional approach to calibrating for the effects of a finite temporal (or spatial) response function is to employ a Fourier deconvolution procedure. This requires precise knowledge of the entire temporal impulse response function (IRF) for every source–detector pair in the system. Although, as will be shown, the calibration measurements detailed in Sec. IV A are sufficient to extract these impulse responses [Eq. (15)], their derivation would require multiple convolution and deconvolution. This procedure would amplify errors and noise, and increase the complexity of preprocessing. However, as shown below, it is possible to recover certain “deconvolved datatypes” from the measured temporal signal without the need to manipulate data in the frequency domain.

Suppose we assume that an experimentally measured TPSF, represented by $y(t)$, can be described as the convolu-

tion of the ideal TPSF $D(t)$ and an impulse response function specific to each source–detector pair $I(t)$:

$$y(t) = D(t) * I(t), \tag{1}$$

where $*$ denotes a convolution and t =time. If we express the convolution integral as a summation, the measured TPSF can be expressed as

$$y(t) = \sum_{\nu} D(t - \nu) I(\nu). \tag{2}$$

If we define the mean flight time of $y(t)$ as

$$\text{Mean}[y(t)] = \frac{\sum_t y(t) \times t}{\sum_t y(t)} \tag{3}$$

and substitute Eq. (2) into Eq. (3) we obtain

$$\begin{aligned} \text{Mean}[y(t)] &= \frac{\sum_t y(t) \times t}{\sum_t y(t)} \\ &= \frac{\sum_t \sum_{\nu} D(t - \nu) I(\nu) t}{\sum_t \sum_{\nu} D(t - \nu) I(\nu)} \\ &= \frac{\sum_x \sum_{\nu} D(x) I(\nu) (x + \nu)}{\sum_x \sum_{\nu} D(x) I(\nu)} \\ &= \frac{\sum_x D(x) \times x}{\sum_x D(x)} + \frac{\sum_{\nu} I(\nu) \times \nu}{\sum_{\nu} I(\nu)}, \end{aligned} \tag{4}$$

where $x = (t - \nu)$. Therefore

$$\text{Mean}[y(t)] = \text{Mean}[D(x)] + \text{Mean}[I(\nu)]. \tag{5}$$

We find that the mean flight time of the measured TPSF is equal to the sum of the ideal mean flight time ($\text{Mean}[D(x)]$) and a quantity equal to the mean time of the instrument’s IRF ($\text{Mean}[I(\nu)]$). Similarly it can be shown that the same is true for the second and third central temporal moments (central variance and skew) where

$$\begin{aligned} \text{Variance}[y(t)] &= \frac{\sum_t y(t) \times (t - \langle t \rangle)^2}{\sum_t y(t)} \\ &= \text{Variance}[D(x)] + \text{Variance}[I(\nu)] \end{aligned} \tag{6}$$

and

$$\begin{aligned} \text{Skew}[y(t)] &= \frac{\sum_t y(t) \times (t - \langle t \rangle)^3}{\sum_t y(t)} \\ &= \text{Skew}[D(x)] + \text{Skew}[I(\nu)]. \end{aligned} \tag{7}$$

For the normalized Laplace transform and integrated intensity datatypes, it can be shown that the ideal datatype is *multiplied* by a factor equal to the datatype of the IRF:

$$\begin{aligned} \text{Intensity}[y(t)] &= \sum_t y(t) \\ &= \text{Intensity}[D(x)] \times \text{Intensity}[I(\nu)], \end{aligned} \tag{8}$$

$$\begin{aligned} \text{Laplace}[y(t)] &= \frac{\sum_t e^{-st} y(t)}{\sum_t y(t)} \\ &= \text{Laplace}[D(x)] \times \text{Laplace}[I(\nu)], \end{aligned} \tag{9}$$

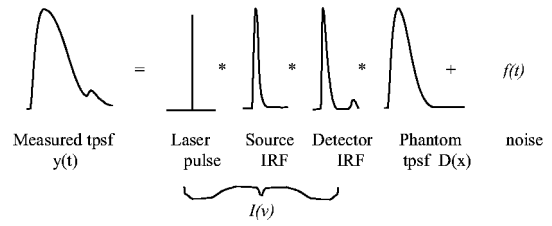


FIG. 5. A measured TPSF can be described as a convolution of the actual TPSF of the object and the impulse response functions (IRFs) of each part of the measurement system, plus nonconvolved noise.

where s =the Laplace coefficient. Thus it is not necessary to measure the whole impulse response of the system in order to obtain the equivalent of the datatypes of a deconvolved TPSF. One can effectively deconvolve the IRF from a datatype by simply subtracting $M[I(\nu)]$ or dividing it by $L[I(\nu)]$, where $M[y(t)]$ is a temporal moment and $L[y(t)]$ is intensity or Laplace. Also, since the above relationships hold for any convolved functions, it is possible to derive these correction values by combining the datatypes of the various calibration measurements described in Sec. IV A. This is appropriate if we make the reasonable assumption that each measured TPSF consists of the ideal TPSF convolved with the temporal response of each individual component of the system used in that measurement. This is illustrated schematically in Fig. 5.

If the additive noise term $f(t)$ is ignored, the mean, variance, and skew datatypes derived from the measured TPSF can be represented by the general expression

$$\begin{aligned} M[y(t)] &= M[\text{laser pulse}] + M[\text{Source IRF}] \\ &\quad + M[\text{Detector IRF}] + M[\text{Ideal TPSF}]. \end{aligned} \tag{10}$$

Thus in order to extract the ideal datatype ($=M[D_{n,m}(t)]$) from the measurement we are required to evaluate $M[I_{n,m}(t)]$ (for n =source number=1–32 and m =detector number=1–32), where

$$\begin{aligned} M[I_{n,m}(t)] &= M[\text{laser pulse}] + M[\text{Source}_n \text{IRF}] \\ &\quad + M[\text{Detector}_m \text{IRF}]. \end{aligned} \tag{11}$$

Let us consider how the source, detector, and absolute calibration measurements described in Sec. IV A can be broken down in this way:

(i) **Source calibration:** The datatype $M[\text{Srcal}_{n,1}(t)]$ of the TPSF collected by detector 1 from source n , with the calibration tool in configuration B, can be expressed as

$$\begin{aligned} M[\text{Srcal}_{n,1}] &= M[\text{laser pulse}] + M[\text{Source}_n \text{IRF}] \\ &\quad + M[\text{Detector}_1 \text{IRF}] + M[\text{Tool}_B \text{TPSF}]. \end{aligned} \tag{12}$$

(ii) **Detector calibration:** The datatype $M[\text{Detc}_{\text{spare},m}(t)]$ of the TPSF collected by detector m from the spare source with the calibration tool in configuration A can be expressed as

$$\begin{aligned} M[\text{Detc}_{\text{spare},m}] &= M[\text{laser pulse}] + M[\text{Source}_{\text{spare}} \text{IRF}] \\ &\quad + M[\text{Detector}_m \text{IRF}] + M[\text{Tool}_A \text{TPSF}]. \end{aligned} \tag{13}$$

(iii) **Absolute calibration:** The datatype $M[\text{Abscal}_{1,1}(t)]$ of the TPSF collected by detector 1 from source 1 using the absolute calibration tool can be expressed as

$$\begin{aligned} M[\text{Abscal}_{1,1}] &= M[\text{laser pulse}] + M[\text{Source}_1\text{IRF}] \\ &\quad + M[\text{Detector}_1\text{IRF}] + M[\text{Tool}_{\text{Abs}}\text{TPSF}]. \end{aligned} \quad (14)$$

By rearranging Eqs. (12), (13), and (14) and substituting into Eq. (11) we obtain

$$\begin{aligned} M[I_{n,m}(t)] &= M[\text{Srcal}_{n,1}] + M[\text{Detcal}_{\text{spare},m}] \\ &\quad - M[\text{Srcal}_{1,1}] - M[\text{Detcal}_{\text{spare},1}] \\ &\quad + M[\text{Abscal}_{1,1}] - M[\text{Tool}_{\text{Abs}}]. \end{aligned} \quad (15)$$

The only value in Eq. (15) which is not directly calculable from the calibration data is $M[\text{Tool}_{\text{Abs}}]$. For mean flight time $M[\text{Tool}_{\text{Abs}}]$ is simply the mean time taken for light to travel the 7 mm distance through air (≈ 23 ps), in the absolute calibration tool shown in Fig. 4. For variance, $M[\text{Tool}_{\text{Abs}}] \approx 0$, since there is negligible temporal broadening of a pulse passing through 7 mm of air.

Subtraction of $M[I_{n,m}(t)]$ from datatypes calculated directly from the uncalibrated data then yields the same result as a deconvolution of the true IRF for that particular source–detector pair (n, m) .

Equation (15) does not hold for the Laplace and intensity datatypes [Eqs. (8) and (9)], where the effect of the impulse response is multiplicative. However, following a similar procedure to that described above, it can be shown that the factor required to correct these datatypes is given by

$$L[I_{n,m}(t)] = \frac{L[\text{Srcal}_n] \times L[\text{Detcal}_m] \times L[\text{Abscal}_{1,1}]}{L[\text{Srcal}_1] \times L[\text{Detcal}_1] \times L[\text{Tool}_{\text{Abs}}]}, \quad (16)$$

where the terms on the right hand side are the corresponding datatypes derived from the calibration measurements, e.g., $\text{Laplace}[y(t)] = L[y(t)]$. Note that in this case $\text{Laplace}[\text{Tool}_{\text{abs}}] \approx \exp(-23 \times s)$.

C. Corresponding interpretation of difference imaging

The results derived above demonstrate why difference imaging is so effective in the removal of systematic errors. If the TPSFs collected are given by

$$\begin{aligned} y_{n,m}(t) &= \text{laser pulse} * \text{Source}_n\text{IRF} * \text{Detector}_m\text{IRF} * \text{Ideal TPSF} \\ &= I_{n,m}(\nu) * D_{n,m}(x), \end{aligned} \quad (17)$$

a full data set collected on a homogeneous phantom under identical conditions to data collected on the object of interest provides an entire set of $I_{n,m}(\nu) * D_{n,m,\text{reference}}(x)$. Thus using Eq. (8), the ratio of intensities from the structured and homogeneous phantoms (or other reference set), will eliminate $I_{n,m}(\nu)$, assuming that it has remained constant between the two acquisitions

$$\begin{aligned} &\frac{\text{Intensity}[y_{\text{object}}(t)]}{\text{Intensity}[y_{\text{reference}}(t)]} \\ &= \frac{\text{Intensity}[D_{\text{object}}(x)] \times \text{Intensity}[I(\nu)]}{\text{Intensity}[D_{\text{reference}}(x)] \times \text{Intensity}[I(\nu)]} \\ &= \frac{\text{Intensity}[D_{\text{object}}(x)]}{\text{Intensity}[D_{\text{reference}}(x)]}, \end{aligned} \quad (18)$$

and similarly for mean flight time

$$\begin{aligned} &\text{Mean}[y_{\text{object}}(t)] - \text{Mean}[y_{\text{reference}}(t)] \\ &= \text{Mean}[D_{\text{object}}(x)] - \text{Mean}[D_{\text{reference}}(x)]. \end{aligned} \quad (19)$$

Using the calibration methods described in Sec. IV B, we are deriving only datatypes of $D_{\text{object}}(x)$, in which case TOAST estimates datatypes for $D_{\text{background}}(x)$ and creates a data set in the form of Eqs. (18) and (19). This accentuates the features of the data due to internal structure above the dominant effects of, for example, source–detector separation. So the successfulness of this type of difference imaging depends on the assumption that $D_{\text{background}}(x) \equiv D_{\text{reference}}(x)$. Alternatively, if the optical properties of the reference object are well known, TOAST could simulate $D_{\text{reference}}(x)$, although a well-matched reference object with identical source–detector geometries may also reduce the effects of systematic errors due to dynamic range, or positional uncertainty (although nonconvolved errors cannot be expected to cancel completely).

If the match between the reference and the object of interest is poor, $D_{\text{reference}}(x)$ will not be sufficiently similar to the $D_{\text{background}}(x)$ term and the reconstruction algorithm will not be able to adequately model the probable corresponding internal structure of the object being imaged. Even if the internal structures of the objects are both simple and similar, mismatches can result in artifact, as will be shown in Sec. V D.

Note however that difference imaging may also be used for more than just calibration. In this case the values of $D_{\text{reference}}(x)$ are significant for assessing, for example, a change in physiological state or for wavelength difference imaging. By combining difference data sets, as shown above, many systematic errors are eliminated, however it is then important to consider the meaning of $L[D_{\text{object}}(x)]/L[D_{\text{reference}}(x)]$, or $M[D_{\text{object}}(x)] - M[D_{\text{reference}}(x)]$. We must assume that: (a) the absolute structure is sufficiently simple that “linearization” can be assumed; and (b) photons have traveled through the same regions in both data sets. As demonstrated by Arridge and Schweiger,¹⁸ without adequate knowledge of the absolute structure of the object, a linearized reconstruction starting from a homogeneous mesh may fail to produce a difference image, for example, if there is a significant region of higher scatter in an object and difference images are acquired before and after an event which results only in an absorption change. In this case the reconstruction will not be able to model the correct paths of photons through the object, so correct localization of the absorption changes is unlikely. As demonstrated by Schweiger and Arridge,¹⁹ photon measurement density functions also depend on μ_a , so in the case of wavelength difference imag-

ing, the paths taken by photons may be sufficiently different, that the photons in each image may not be probing the same regions. Again this would prohibit adequate image reconstruction.

Difference imaging is therefore successful since, as shown above, it provides data where many systematic errors have cancelled. This may account for the impressive image quality apparently achievable. However we have also shown that poor matching of the object and reference will significantly degrade the effectiveness of the method. This is particularly important when imaging clinical subjects where shape, structure, and optical properties are unknown, and in the case of subjects with specific pathologies, may be significantly different from what may normally be expected.

D. Reduction of the effects of nonconvolved noise

The effectiveness of the deconvolution-equivalent technique described in Sec. IV B, and indeed difference imaging depends on the influence of the additive noise term illustrated in Fig. 5. Stochastic noise and cross talk are not convolved functions. Higher order moments such as skew are heavily dependent on such noise and its effects may overwhelm the corrections calculated for individual source–detector combinations. Noise on calibration TPSFs may have far more effect on the datatype derived than the shape or temporal position of the calibration TPSF, hence limiting the usefulness of the subsequent calibration. Although stochastic noise and cross talk can be reduced via hardware alterations, processing for remaining nonconvolved features is necessary.

1. Low pass filtering

High frequency noise removal using a low pass filter is inappropriate as a method of removing stochastic noise. This is because a low pass filter is simply a multiplication of the Fourier transform of the data to be filtered by a chosen window $H(\omega)$ in the frequency domain. In turn, this represents the convolution of a shift-invariant function $h(t)$ (the inverse Fourier transform of the window) in the time domain. As demonstrated by Eqs. (5), (6), (7), (8), and (9), datatypes derived from a TPSF $y(t)$ that has been convolved with a function $h(t)$ will equal the original TPSF's datatypes ($M[y(t)]$ or $L[y(t)]$) either with a constant $M[h(t)]$ added (for moments), or multiplied by a constant $L[h(t)]$ (for intensity and Laplace). If the low pass filter chosen is an even function, subsequently derived intensity and Laplace datatypes will simply all be scaled by a constant factor, and even moments (e.g., variance) will all be offset by a constant amount. Mean and skew (the odd moments) will be unaffected and in all cases the effects of the stochastic noise will remain. However, potentially, high frequency spikes on TPSFs could be removed using a “median filter,” which may help to reduce spurious errors in higher order datatypes.

2. Background subtraction

A background subtraction scheme will reduce the effects of a constant offset on datatypes, such as that due to the level of stochastic noise on a particular TPSF (dependent on the signal intensity and the properties of the detector). Because

of the prepeak (Sec. II B), signal recorded at the shortest flight times does not provide a reliable measure of the background noise. Instead, the background noise is sampled at the largest flight times, following the region containing the main TPSF. The last 160 data points are averaged into 16 bins (10 data points=50 ps). The lowest value bin is then assumed to represent the background level. This method also avoids the possibility of including the reflection peak (Sec. II C) within the calculation of background intensity. The background level value is subtracted from every data point in the TPSF automatically and before extraction of datatypes. The low frequency background variation due to cross talk in the eight-anode MCPs (Sec. II B), may continue to affect datatypes following “constant background” subtraction. However it may be possible to adequately predict the magnitude and temporal position of such cross talk, if the fraction of cross talk occurring can be measured and assumed to remain constant.

3. Dynamic windowing

Appropriate selection of the range over which to calculate a datatype from a TPSF can reduce the effects of the varying amounts of stochastic and other systematic noise on either side of the TPSF. This is particularly important for the central moments (variance and skew), which are more dependent on photons far from the mean of the TPSF. In addition, for effective application of the calibration procedures described in Sec. IV B and for difference imaging as described in Secs. III A and IV C, the derivation of datatypes from the main data set and the calibration or reference data sets should be equivalent. This is because we are effectively canceling out *sums over time t* [see Eqs. (3)–(9)] and the limits of these sums should be the same for all relevant calculations. The temporal window also ensures that any reflections or other temporal features specific to the source–detector pair are included in the calculation of calibration values, if they have influenced the datatype values derived from the actual data TPSF.

We must define this temporal window, over which to calculate datatypes, as the time either side of a fixed point. Although it requires the assumption that the MONSTIR TPSFs are approximately symmetric, the mean flight time has been chosen as this anchor point, since it is easier and more reliable to calculate than peak position. Hence we need an iterative procedure for derivation of the mean flight time datatype since the mean of the TPSF is required to deduce the window over which to calculate a better estimate of the mean flight time. Once the optimal window for a particular TPSF has been deduced, this same distance either side of the mean flight time of each calibration TPSF is used to calculate the “calibration datatypes.”

Once the mean flight times have been calculated, it is possible to deduce absolute time=0 using Eq. (15). This allows further refinement of the window since we can eliminate the inclusion of any apparent photon counts prior to either the entrance time of photons ($t=0$) or the ballistic photon time [$t=\text{source detector separation}/(c/n)$], where $c=\text{speed of light}$ and n is the refractive index. The ballistic photon start time is used to establish the window for calcu-

lation of the Laplace datatype since it is particularly sensitive to early photons, and hence the prepeak. Since central skew is an odd function, the use of a symmetric window either side of the TPSFs mean should aid cancellation of high frequency random noise. If the ballistic photon time is known, the section of data containing the prepeak could be replaced with a section of background noise from the end of the TPSF to constitute the datatype calculation window extending an equal distance before and after the mean. Since central variance is an even function, it is desirable to calculate the datatype over as small a window as possible, while not truncating the tail of the TPSF. Intensity and mean flight time should be least susceptible to high frequency random noise, since its integral should tend to zero. It is important though to consider the effects of the prepeak, and of low frequency noise components such as MCP cross talk that may not effectively cancel over the window.

V. USING A TWO-DIMENSIONAL RECONSTRUCTION SCHEME TO PRODUCE IMAGES

A. Reconstruction considerations

If we are attempting to develop a general calibration method, we are in effect trying to produce calibrated data that matches the 3D TOAST forward model. Development of the TOAST reconstruction software naturally began with the optimization of 2D meshes and reconstruction methods, prior to development of the 3D methods that are now being optimized.²⁰ So far, all experiments conducted with MONSTIR have utilized sources and detectors confined to a single plane (as shown in Fig. 1). As a consequence it has been tempting to suppose that reconstruction could be achieved using an algorithm that is likewise limited to 2D. However, since photons are free to migrate in all three dimensions within a scattering medium, measurements made at the surface are inevitably affected by photons that have traveled through structure located above and below the plane of interest. Although this sensitivity will decrease quite rapidly with increasing distance from the plane (depending on the attenuation of the object), not only will out-of-plane structure influence images, but also quantitation will undoubtedly be affected. We must hence employ a 3D forward model if quantitative imaging is required. The importance of including 3D information in order to provide accurate quantitative information has already been demonstrated by Cheng and Boas.²¹

Regardless of the effects of out-of plane structure however we have also found that the statistical distribution of photon flight times between two points for 2D and 3D models are sufficiently dissimilar to produce a significant difference in the forward model predictions of the datatypes. This is illustrated in Fig. 6, which shows TPSFs generated using 2D and 3D FEM models for a homogeneous disk and a cylinder of equal diameter (70 mm). Both models employ the same transport scattering coefficient ($\mu'_s = 1.0 \text{ mm}^{-1}$), absorption coefficient ($\mu_a = 0.01 \text{ mm}^{-1}$), and source–detector separation ($d = 70 \text{ mm}$). The differences between the TPSFs suggest that datatypes derived from a 2D FEM model are

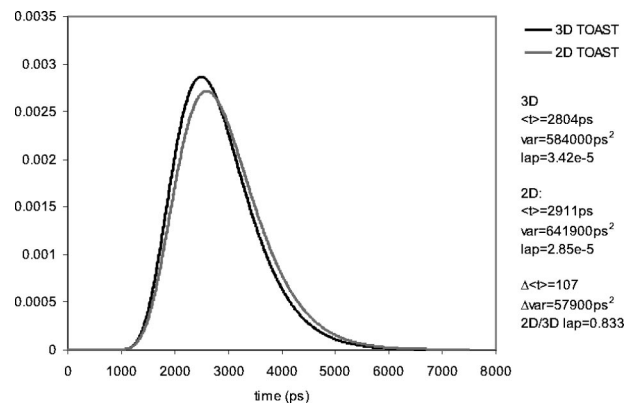


FIG. 6. TPSFs generated by TOAST forward models using either 2D (circular) or 3D (cylindrical) meshes, of diameter 70 mm. Both are homogeneous $\mu'_s = 1.0 \text{ mm}^{-1}$ and $\mu_a = 0.01 \text{ mm}^{-1}$, and have a source–detector separation of 70 mm. The values for the mean time, variance, and Laplace for each TPSF are also shown.

likely to be significantly different from those acquired experimentally.

Nevertheless, 2D models are very attractive since computation is substantially faster. Consequently we have examined the possibility of applying an appropriate correction to experimental data in order to render it more suitable for a 2D algorithm. Such a correction would not be capable of eliminating the effects of out-of-plane structure. However if a series of 2D images, representing slices of a 3D object, can be clearly reconstructed thanks to a derived correction factor, it is possible to deduce aspects of the 3D structure by comparing adjacent images, as demonstrated by Schmidt *et al.*²² A preliminary exploration of the feasibility of deriving a correction factor was conducted by Schweiger and Arridge, who employed data simulated using a 3D FEM model.²³ Image reconstructions based on the uncorrected data and a 2D algorithm exhibited a significant ring artifact. The simulated data were then adjusted by rescaling each datatype by a factor dependent on the source–detector separation. These factors were generated by dividing the datatype derived from a 3D FEM model of a homogeneous cylinder by the same datatype generated from a 2D FEM model of a homogeneous disk of the same diameter and optical properties. This crude correction method produced images with significantly less artifact.

If we are to investigate the effectiveness of such corrections, since the 2D and 3D FEM models must utilize optical properties as close as possible to those of the object, a protocol for extracting the average values of these properties from experimental data had to be developed.

B. Estimation of average background optical properties

Although analytic solutions to the diffusion approximation for a cylinder and a circle exist,²⁴ it is not straightforward to invert them to derive optical properties from boundary data. The simple analytical approach described here is to deduce the average background optical parameters of the object being imaged from the average datatype for each source–detector spacing. An initial guess of the relation be-

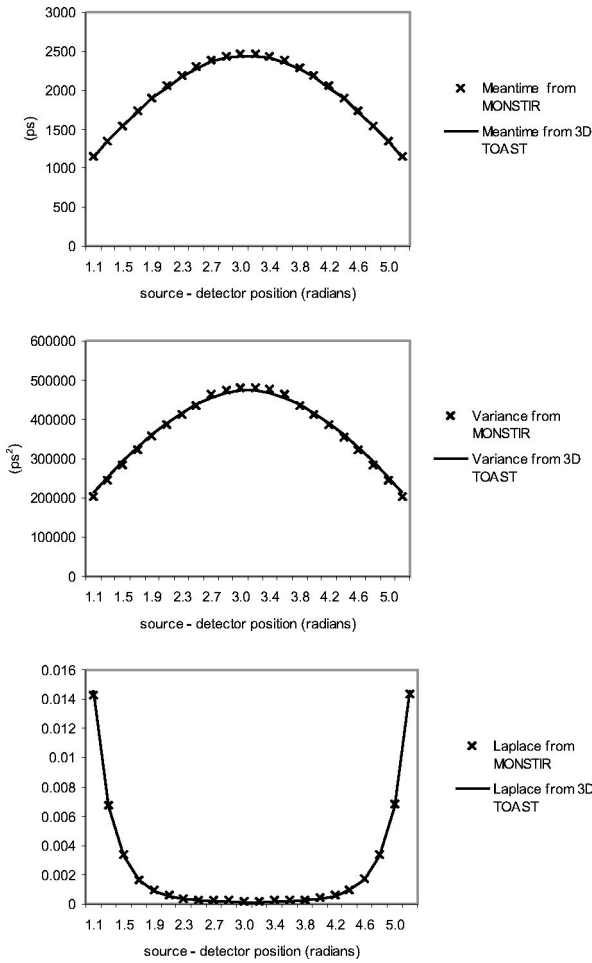


FIG. 7. Comparison of the datatypes calculated from experimental TPSFs to datatypes from a TOAST 3D forward model. The datatypes are the averages for each source–detector spacing, extracted from experimental TPSFs collected on a solid cylindrical phantom, diameter 70 mm, and have had the methods described in Secs. IV A, IV C, and IV D applied to compensate for the individual IRFs of the system. The forward model used a 3D cylindrical mesh of the same dimensions as the phantom, with optical properties deduced using the method described in Sec. IV B ($\mu'_s = 0.85 \text{ mm}^{-1}$ and $\mu_a = 0.011 \text{ mm}^{-1}$ at 800 nm).

tween μ_a and μ'_s can be made to within $\pm 10\%$ from a least squares fit to mean flight time versus source–detector spacing for separations of >50 mm. If the gradient of this fit is M , using the 3D infinite space Green’s functions [see Eq. (A6)] it can be shown that

$$\mu'_s \approx \left(\frac{4M^2 c^2}{3n^2} - 1 \right) \mu_a, \quad (20)$$

where c = speed of light and n = refractive index of the object. However the absolute values of Laplace and variance calculated via the infinite space Green’s functions are found to be far more sensitive to the infinite space approximation. Thus Green’s functions are ineffective in retrieving further information about the values of μ_a and μ'_s . Instead we use a ‘look-up table’ of 3D FEM datatypes to deduce the values of μ_a and μ'_s that agree with Eq. (20), and that also give consistent agreement with experimental and forward model predictions of variance and Laplace. This also offered confirmation that the datatype calibration procedures in Sec.

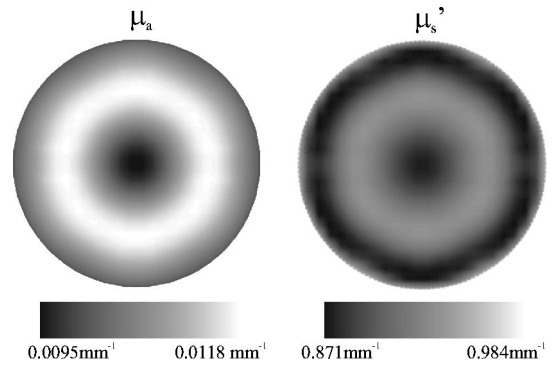


FIG. 8. Reconstructions of μ'_s and μ_a showing the effect of a constant offset in mean time and variance, and a constant scaling of Laplace, as described in Sec. V C. The datatypes were derived using a 2D TOAST forward model, manipulated, and then reconstructed on the same 2D mesh.

IV B provided datatypes consistent with a unique set of μ_a and μ'_s (see Fig. 7). Creation of a full look-up table for many geometries and optical properties would allow swift and automated deduction of average properties by seeking values that simultaneously minimize the error between each simulated and experimental datatype.

C. Calculation of correction factors

The generation of appropriate correction factors has been investigated using both FEM, and Green’s function solutions to the 2D and 3D diffusion equation for an infinite medium²⁴ [see Eqs. (A1) and (A2)]. An empirical examination of the Green’s function analytical models yielded several interesting discoveries. First, datatypes calculated from 2D and 3D Green’s functions for identical optical properties and source–detector separations were evidently very different. Second, the 2D:3D *difference* between some datatypes (mean flight time, variance, and skew) were virtually independent of source–detector separation. This indicates that ‘correction’ of these datatypes could be achieved by simply *adding* a constant value. Third, the *ratio* of other datatypes (intensity and Laplace) were likewise reasonably independent of source–detector separation, suggesting that correction could be achieved by simply *multiplying* each datatype by a constant value (assuming negligible boundary effects). This is behaviorally consistent with the properties of the datatypes derived in Sec. IV B.

It is perhaps counterintuitive that a factor independent of source–detector spacing will result in a ring artifact. To examine this, we used a 2D forward model (homogeneous, $\mu'_s = 0.9 \text{ mm}^{-1}$ and $\mu_a = 0.01 \text{ mm}^{-1}$, diameter 70 mm) to simulate a set of datatypes. We then subtracted a constant offset (120 ps and 60 000 ps²) from all mean flight time and variance datatypes, respectively, divided all Laplace datatypes by 0.55, and then reconstructed on the same 2D mesh. The constants were chosen to mimic the 2D:3D mismatch. The resulting images for μ_a and μ'_s at iteration 8 both exhibit characteristic ring artifacts as shown in Fig. 8.

For the calculation of correction factors using FEM models, it is essential that the 3D model employs a mesh with the highest possible resolution. This is because coarser meshes are inherently less accurate, and a strong dependence

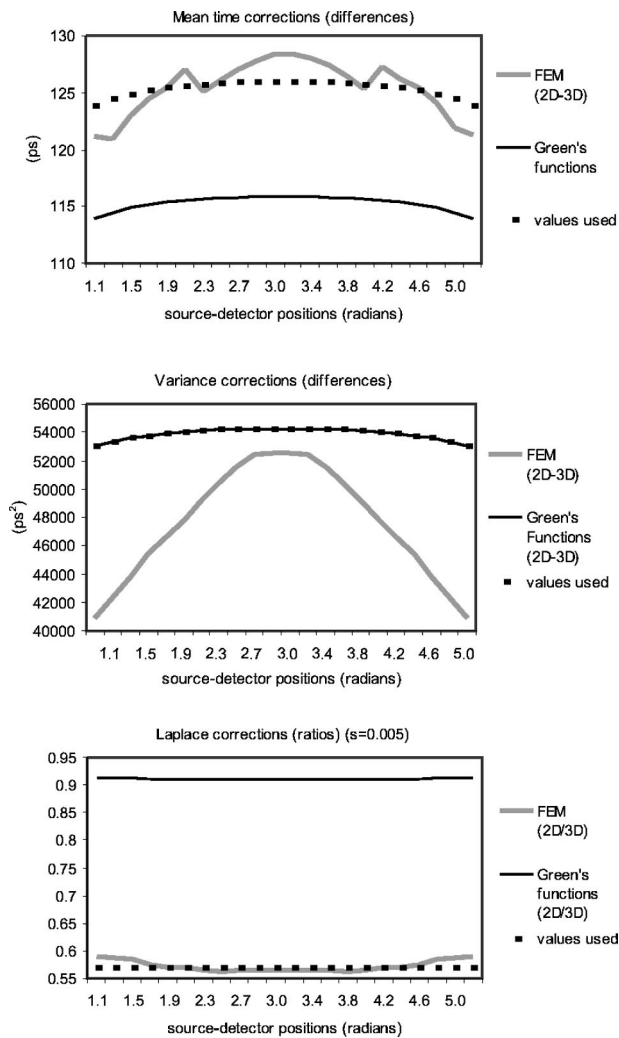


FIG. 9. Correction values for mean time, variance, and Laplace to compensate for the 2D:3D mismatch, calculated using Green's function, FEM forward models, and the values found to be effective for reducing artifact.

between datatype values and mesh resolution is observed if the mesh is insufficiently fine. However, if we are attempting to reduce the mismatch between experimental data and the 2D forward model, it follows that the 2D mesh employed in the correction should be the same as that used for the image reconstruction of experimental data.

Despite the promising results achieved earlier with this approach,²³ close inspection of the correction factors generated from ratios of FEM datatypes reveals an irregularity in the relationship between the correction factors and source-detector separation. This effect is possibly due to the subtle dependencies of finite element calculations on the resolutions of the 2D and 3D meshes. This irregularity is illustrated in Fig. 9. Datatype correction using factors that exhibit this irregularity may cause additional artifacts in the reconstructed images.

Because the Green's function models are only strictly valid for an infinite diffusing medium, the absolute values of correction factors are unlikely to be similar to those generated using finite media of arbitrary geometry. This was confirmed by comparing Green's function correction factors with those derived from FEM models. However, corrections

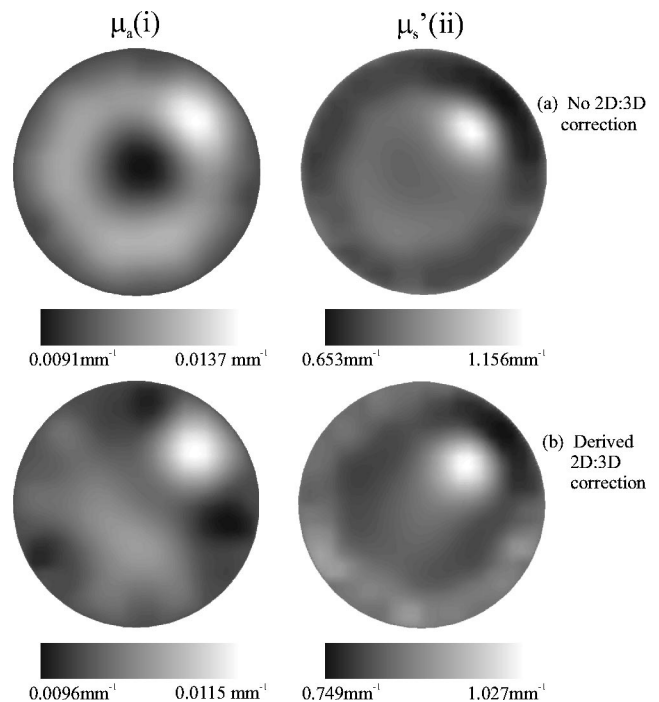


FIG. 10. (a) Reconstruction of experimental data using a 2D mesh with no 2D:3D correction. (b) Reconstruction of experimental data using a 2D mesh with the corrections derived and applied as described in Sec. V C.

derived using both methods have relatively little dependence on source-detector separation, and experiments using many potential corrections indicated that it is the absolute magnitude of the correction that is most critical in achieving artifact reduction. Indeed, once the optimal absolute value had been deduced, simply adding a constant to all temporal data, and multiplying the Laplace data by a constant could significantly reduce ring artifacts (the exact converse of Fig. 8). Hence our method-of-choice involves rescaling the correction factors obtained from the infinite space Green's function ratios so that their values agree roughly with the FEM-derived factors. The correction factors are then applied to the data using the sum-or-multiply rules for each datatype as suggested by the Green's function results. The Green's function, FEM, and the final 2D:3D correction values chosen for mean flight time, variance, and Laplace are shown in Fig. 9.

D. 2D:3D correction in difference imaging

If a difference image, as described in Sec. IV C, is reconstructed using a 2D mesh, the artifact due to a 2D:3D mismatch is not evident (see Fig. 3). Since both the reference and the image data set will have common features due to 3D propagation, the resulting offsets are likely to cancel as suggested by Schweiger and Arridge.²³ Note, however, that the effectiveness and applicability of the reference measurement is constrained by the requirement that the geometrical and optical properties of the reference object are well matched to the object of interest, as discussed in Sec. IV C. For example, in this case a reasonable difference in optical properties would result in differences in the absolute magnitudes of the 2D:3D mismatch, so the offsets would not cancel, which would result in artifacts like those seen in Fig. 8.

VI. RESULTS AND DISCUSSION

In Fig. 10, images are presented of the object described in Sec. III A. The data set that was used in combination with reference data to produce the images in Fig. 3, is now reconstructed without the use of the reference measurement, but calibrated using the methods described in Secs. IV A, IV B, and IV D. The images are all iteration 8, the same FEM mesh and starting parameters were used as for the images in Fig. 3, and the images are scaled linearly from the minimum to the maximum pixel values.

To demonstrate the effect of applying the 2D:3D correction described in Sec. V C, Fig. 10(a) shows images of absorption and scatter reconstructed using a 2D mesh. Mean flight time, variance, and Laplace datatypes were derived from the experimentally collected TPSFs and calibrated using the methods described in Secs. IV A, IV B, and IV D. Without the 2D:3D correction, a ring artifact is evident which is very similar to that apparent in Fig. 8.

Figure 10(b) shows the images that have been generated after application of the 2D:3D correction factors to the datatypes used for Fig. 10(a). The central ring artifact has been significantly reduced, and the embedded object can clearly be identified. In each case, the eighth iteration of the reconstruction algorithm is shown, since qualitatively the images are superior to later iterations; Although quantitation improves in later iterations, without regularization the artifacts on the boundary tend to worsen.

In comparison with the difference images shown in Fig. 3, the images in Fig. 10(b) do exhibit more artifact. Also, the positions of the μ'_s and μ_a features are slightly different in Figs. 10(b)(i) and 10(b)(ii), where their positions agree more closely in Fig. 3. This suggests that the effect of the 2D:3D match has not been fully accounted for by the derived correction. There is also more nonsymmetric artifact in Fig. 10(b) than in Fig. 3, indicating that some differences between sources and detectors have not been completely accounted for by the calibration procedures described in Secs. IV A, IV B, and IV D, as compared to difference imaging.

Undoubtedly, reconstructions Fig. 10(b) are of poorer quality than the difference images in Fig. 3. Importantly however, in principle, the calibration measurements and techniques used to produce the images in Fig. 10 can be applied to data acquired on objects of virtually any shape and optical properties, without requiring a specially constructed reference phantom. The calibration measurements are quicker to acquire than a complete image data set on a matched reference phantom, and the preprocessing required is fast and simple, all of which improve the applicability of the calibration methods to the clinical environment. If the 2D:3D correction is not applied, the calibrated data are suitable for reconstruction on a 3D mesh. So if the effects of out-of-plane structure render the 2D:3D correction inadequate, images can still be produced without requiring the use of a reference object.²⁰

Understanding the origins of errors in derived datatypes, and attempting to account for them, has yielded images whose quality is approaching that achievable via difference imaging, and promises to produce further improvements to

image quality as further corrections are applied. In addition the capabilities of the TOAST reconstruction algorithm have not been fully exploited in this article; other datatypes (e.g., Mellin–Laplace¹²), regularization, the inclusion of *a priori* knowledge (e.g., from a MRI scan),²⁵ higher order FEM meshes, and faster 3D reconstructions²⁰ are all being developed.

ACKNOWLEDGMENTS

For further details about this work and the availability of our software, data, and phantoms see <http://www.medphys.ucl.ac.uk/research/borg>. Support for this research has been generously provided by The Wellcome Trust, The UCL Graduate School, Action Research, EPSRC, and Hamamatsu Photonics.

APPENDIX

The infinite space 3D Green's function solution to the diffusion approximation to the radiative transfer equation²⁴ is

$$G_{3D}(\omega) = \frac{3(\mu_a + \mu'_s)}{2d(2\pi)^{3/2}} e^{-d\sqrt{3(\mu_a + \mu'_s)[\mu_a + (i\omega/c)]}}, \quad (A1)$$

where ω is frequency, μ_a is the absorption coefficient, μ'_s is the transport scattering coefficient, d is the source–detector spacing, and c is the speed of light in the medium. The corresponding 2D form is

$$G_{2D}(\omega) = \frac{3(\mu_a + \mu'_s)}{2(2\pi)^{3/2}} \times K_0 \left[\sqrt{3d} \sqrt{(\mu_a + \mu'_s) \left(\mu_a + \frac{i\omega}{c} \right)} \right], \quad (A2)$$

where $K_0[]$ is the modified Bessel function of order zero. The datatypes discussed in this article can be described by

$$\text{Mean flight time} = \frac{i \frac{\partial G(\omega)}{\partial \omega} \Big|_{\omega=0}}{G(0)}. \quad (A3)$$

Variance (about the mean)

$$= \frac{-\frac{\partial G(\omega)}{\partial \omega} \Big|_{\omega=0}}{G(0)} - \left(\frac{i \frac{\partial G(\omega)}{\partial \omega} \Big|_{\omega=0}}{G(0)} \right)^2, \quad (A4)$$

$$\text{Laplace} = \frac{G(\omega) \Big|_{\omega=0, \mu_a = \mu_a + s}}{G(0)}, \quad (A5)$$

where s is the Laplace coefficient. So for example using the 3D Green's function ($G(\omega) = G_{3D}(\omega)$) we get

$$\text{Mean flight time} = \frac{\sqrt{3}nd(\mu_a + \mu'_s)}{2c\sqrt{\mu_a(\mu_a + \mu'_s)}}. \quad (A6)$$

¹F. F. Jobsis, *Science* **198**, 1264 (1977).

²M. S. Patterson, B. Chance, and B. C. Wilson, *Appl. Opt.* **28**, 2331 (1989).

³D. T. Delpy and M. Cope, *Philos. Trans. R. Soc. London, Ser. B* **352**, 649 (1997).

- ⁴S. R. Arridge and W. R. B. Lionheart, *Opt. Lett.* **23**, 882 (1998).
- ⁵F. E. W. Schmidt, M. E. Fry, E. M. C. Hillman, J. C. Hebden, and D. T. Delpy, *Rev. Sci. Instrum.* **71**, 256 (2000).
- ⁶M. Schweiger and S. R. Arridge, *OSA TOPS Adv. Opt. Imaging and Photon Migration* **2**, 263 (1996).
- ⁷S. R. Arridge, *Inverse Probl.* **15**, R41 (1999).
- ⁸B. W. Pogue, M. S. Patterson, H. Jiang, and K. D. Paulsen, *Phys. Med. Biol.* **40**, 1709 (1995).
- ⁹T. M. McBride, B. W. Pogue, E. D. Gerety, S. T. Poplack, U. L. Österberg, and K. D. Paulsen, *Appl. Opt.* **38**, 5480 (1999).
- ¹⁰H. Jiang, K. D. Paulsen, U. L. Österberg, and M. S. Patterson, *Phys. Med. Biol.* **43**, 675 (1998).
- ¹¹Y. Ueda, K. Ohata, M. Oda, M. Miwa, Y. Yamashita, and Y. Tsuchiya, *Jpn. J. Appl. Phys., Part 1* **37**, 2717 (1998).
- ¹²M. Schweiger and S. R. Arridge, in *Information Processing in Medical Imaging (IPMI'97)*, Lecture Notes in Computer Science, Vol. 1230 (Springer, New York, 1997), pp. 71–84.
- ¹³M. Schweiger and S. R. Arridge, *Phys. Med. Biol.* **44**, 1699 (1999).
- ¹⁴F. Bevilacqua, D. Pignatelli, P. Marguet, J. D. Gross, B. J. Tromberg, and C. Depeursinge, *Appl. Opt.* **38**, 4939 (1999).
- ¹⁵H. Eda, I. Oda, Y. Ito, Y. Wada, Y. Tsunazawa, and M. Takada, *Rev. Sci. Instrum.* **70**, 3595 (1999).
- ¹⁶V. Ntziachristos, B. Chance, and A. G. Yodanis, *Opt. Express* **5**, 230 (1999).
- ¹⁷V. Ntziachristos, X. Ma, and B. Chance, *Rev. Sci. Instrum.* **69**, 4221 (1998).
- ¹⁸S. R. Arridge and M. Schweiger, *Proc. SPIE* **2389**, 378 (1995).
- ¹⁹M. Schweiger and S. R. Arridge, *Proc. SPIE* **2389**, 366 (1995).
- ²⁰S. R. Arridge, J. C. Hebden, M. Schweiger, F. E. W. Schmidt, M. E. Fry, E. M. C. Hillman, H. Dehghani, and D. T. Delpy, *Int. J. Imaging Syst. Technol.* **11**, 2 (2000).
- ²¹X. Cheng and D. A. Boas, *Opt. Express* **4**, 299 (1999).
- ²²F. E. W. Schmidt, J. C. Hebden, E. M. C. Hillman, M. E. Fry, M. Schweiger, S. R. Arridge, and D. T. Delpy, *Appl. Opt.* **39**, 3380 (2000).
- ²³M. Schweiger and S. R. Arridge, *Appl. Opt.* **37**, 7419 (1998).
- ²⁴S. R. Arridge, M. Cope, and D. T. Delpy, *Phys. Med. Biol.* **37**, 1531 (1992).
- ²⁵M. Schweiger and S. R. Arridge, *Phys. Med. Biol.* **44**, 2703 (1999).